Spectral performance of a zero-order liquid-crystal polymer commercial *q*-plate for the generation of vector beams at different wavelengths

María M. Sánchez-López[1], Isaiah Abella[2], Daniel Puerto-García[3], Jeffrey A. Davis[2], and Ignacio Moreno[4]

[1] Instituto de Bioingeniería. Departamento de Física y Arquitectura de Computadores, Universidad Miguel Hernández, 03202 Elche, Spain

[2] Department of Physics. San Diego State University, San Diego, CA 92182-1233, USA

[3] Ilice Photonics, Parque Científico Empresarial UMH, 03202 Elche, Spain

[4] Departamento de Ciencia de Materiales, Óptica y Tecnología Electrónica, Universidad Miguel Hernández, 03202 Elche, Spain

Abstract.

Liquid-crystal polymer *q*-plates are commercial devices for generating vector beams at the design wavelength where the device exhibits half-wave (HW) retardance. Since they are not voltage addressable, the operational wavelength remains fixed. In this work we perform a broadband spectral characterization of the *q*-plate retardance as a function of wavelength, $\phi(\lambda)$, and identify the wavelengths with retardance values relevant for vector beam generation (π, $\pi/2$, and $3\pi/2$). The wavelength is then used as a tuning parameter to change the device performance from a HW q-plate to a positive-QW or a negative-QW *q*-plate. These performances are analyzed using the Jones matrix formalism. We present a simple procedure to derive the polarization distribution of the vector beams expected at these QW wavelengths, as a superposition of the input polarization state and the output state of a HW *q*-plate. Experimental results using the red and blue lines of an Ar-Kr laser and an IR laser diode of 980 nm confirm the theoretical predictions. We show that for input linearly polarized light of 980 nm and 488 nm the device generates hybrid vector beams (where the ellipticity varies with the azimuthal angle), while for 647 nm pure radial vector beams with constant ellipticity are obtained. These results could extend the use of commercial *q*-plates for multicolour vector beam applications.

Keywords: Q-plates, Vector Beams, Spectral retarders, Orbital Angular Momentum, Space-variant phase retarders.

Corresponding Author: María del Mar Sánchez-López,

E-mail: mar.sanchez@umh.es

1. INTRODUCTION

Q-plates are spatially-variable retarders whose optical axis rotate with the azimuthal angle and act as polarization converters [1-4]. These anisotropic inhomogeneous retarders have become very popular since they impart orbital angular momentum to circularly polarized light and generate cylindrically polarized vector beams [5], this last being the reason why they are also called vector vortex retarders. Vector beams are of great interest for a number of applications; for example, the nonseparability of their space and polarization degrees of freedom can be used to encode information for optical communication [6]. Also, if combined with axicon lenses, their intensity distribution is that of a non-diffracting Bessel beam [7] and the spatially varying states of polarization can be varied upon propagation [8], which makes these beams very useful for materials processing, microscopy and particle manipulation. Therefore, *q*-plates find applications in fields such as classical and quantum communications [9, 10], optical trapping [11, 12], polarization-based spatial filtering [13] and materials processing, where a master *q*-plate provides the illumination redistribution needed to fabricate an offspring *q*-plate retarder with enhanced performance for astronomy and display applications [14].

Q-plates can be made of birefringent liquid–crystal polymers and are available either with a continuous rotation of its optical axis [14, 15] or with segmented sectors [2, 16, 17]. They have also been fabricated by laser-writing of subwavelength structures in non-necessarily birefringent materials (typically silica glass) to yield an effective birefringence [3, 18-20]. Therefore, the inhomogeneous anisotropy of *q*-plates can stem from the birefringent material itself or it can be just structural.

In both cases, the device displays retardance dispersion, i.e. the retardance changes with wavelength as a function $\phi(\lambda)$. Full polarization conversion of the input homogeneously polarized beam into the higher-order vector beam occurs when the retardance is an odd integer multiple of π radians. In this situation, the device converts one circularly polarized light completely into the opposite circular polarization, with an additional helical phase whose sign depends on the input

helicity. Otherwise, the polarization conversion efficiency is reduced as $\sin^2(\phi/2)$ [4, 16], and the device transforms only some fraction of transmitted light and the rest remains in its original state. Therefore, *q*-plates are usually operated as half-wavelength spatially-variable retarders to achieve the maximum efficiency conversion for a design wavelength, which is typically in the visible or in the IR range.

In some cases, fine-tuning of the *q*-plate retardance at odd multiples of π is required for the operating wavelength, and liquid-crystal *q*-plates with thermal [21] or electrical tuning [15-17] are advantageous, where the latter have a faster response of a few tens of miliseconds. The use of a tunable liquid-crystal *q*-plate and a supercontinuum laser has proved the generation of coherent multicoloured vector beams with potential applications in broadband multiplexing and superresolution microscopy [22].

Off-tuned *q*-plates (where $\phi \neq \pi$) are seldomly employed. Their action is made of two terms [4,13]: the amplitude of one is proportional to $\cos(\phi/2)$ and leaves the beam unaffected. The second is proportional to $\sin(\phi/2)$ and implements a helical phase ($\pm 2q\theta$), where θ is the azimuthal coordinate (the sign depends on the input polarization helicity) while changing the handedness of the circular polarization component of the input beam. This superposition has been recently applied in a complex quantum system to implement photonic quantum walks for quantum simulation studies, where the *q*-plate retardance ϕ controls the mobility of the walker [23]. Otherwise, retardances different from π have not attracted a great deal of interest. Only the particular case of quarter-wave retardance has been reported in a few works [18, 24]. The most remarkable feature of these quarter-wave *q*-plates is that the vector beam generated is an equal-weight superposition of the input beam and the vortex beam generated by a tuned *q*-plate. In this situation, radially or azimuthally polarized beams are generated when the *q*-plate is illuminated with circularly polarized light, but only one of the two circular components of this beam exhibits a vortex. These pseudo-radial (pseudo-azimuthal) vector beams have been demonstrated with metamaterial *q*-plates

fabricated by laser-writing on fused silica [18, 24], or by cascading a regular half-wave (HW) *q*-plate with a spiral-phase plate [25]. The operation wavelength is set on fabrication.

In this work, we explore the use of a *q*-plate fabricated as a zero-order half-wave vortex retarder (Thorlabs, model WPV10-633, with *q*=1) to generate vector beams at different wavelengths. This is a commercial *q*-plate based on liquid-crystal polymer, which is not electrically activated and, consequently, not tunable. We use the fact that these retarders show retardance dispersion, $\phi(\lambda)$ and examine the wavelengths at which the retardance is π, $\pi/2$ and $3\pi/2$, since these are the most relevant values for vector beam generation. For that purpose, we perform a broadband spectral characterization of the device retardance. The characterization of the *q*-plate retardance is typically made by measuring their normalized transmittance when placed in between crossed circular polarizers [16, 17]. However, since a broadband light source is used, achromatic circular polarizers are required. We used circular polarizers consisting in a broadband linear polarizer combined with a quarter-wave Fresnel rhomb, a type of retarder that shows negligible dispersion in a broad spectral range. We show that the *q*-plate works as a zero-order retarder, thus providing a relatively large band where it offers good polarization conversion efficiency since the retardance is very close to π radians. However, as we measure the retardance function $\phi(\lambda)$ in a relatively large spectral range (from 400 to over 1000 nm), we can identify other wavelengths where the retardance is $\pi/2$, around 1000 nm, or $3\pi/2$ around 480 nm.

We develop a comprehensive description of the device performance as a quarter-wave (QW) *q*-plate, where we introduce a simple pictorial procedure to obtain the polarization distribution across the beam section. This model is used to interpret the experimental results. The intensity patterns of the vector beams obtained for the six cardinal input polarization states, and captured for the corresponding six polarization analyzers are shown at the three characteristic wavelengths identified for this device. The experimental results are obtained using the red and blue line of an Ar-Kr laser and an IR laser diode.

The possibility of operating a commercial non-tunable *q*-plate at these various wavelengths is interesting since the following vector beams can be generated: 1) when illuminated with circularly polarized light, it yields slanted pseudo-vector beams and, 2) when illuminated with linear polarization, we get hybrid vector beams, where the ellipticity changes with the azimuth angle. Therefore, this work demonstrates the versatility of a zero-order HW *q*-plate for generating vector beams not only at the design wavelength, but also at wavelengths where the device shows quarter-wave retardance. These results could extend the application of these devices; for example in coherent multicoloured vector beam multiplexing, or using it in tandem with a spatial light modulator to generate multicolour hybrid vector beams with tailored orbital angular momentum [26]. Recently, multicolour vector beams using a voltage tunable *q*-plate were reported suitable for stimulated emission depletion microscopy [27]. The use of commercial static q-plates as an alternative device could thus be explored.

2. Q-PLATE THEORY

Next we briefly review the *q*-plate theory. The *q*-plate consists of a phase plate retarder with retardance ϕ where its principal axis follows *q* times the azimuthal angle. Q-plates with a nonlinear azimuthal distribution of the principal axis are also possible and we have recently shown their feasibility to encode binary data [28]. But in this work we consider the standard (commercially available) q-plate, whose Jones matrix can be expressed as [4, 16]:

$$\mathbf{M}_q(\phi) = \cos\left(\frac{\phi}{2}\right)\mathbf{I} + i\sin\left(\frac{\phi}{2}\right)\mathbf{Q}_q . \tag{1}$$

Here $\mathbf{I}$ stands for the identity matrix and $\mathbf{Q}_q$ is the matrix of the *q*-plate tuned at π retardance (HW *q*-plate) which is given by:

$$\mathbf{Q}_q = \begin{pmatrix} \cos(2q\theta) & \sin(2q\theta) \\ \sin(2q\theta) & -\cos(2q\theta) \end{pmatrix}, \tag{2}$$

where θ is the azimuthal angle, and q is the number of rotations that the principal axis performs in a complete cycle of the azimuth. The topological charge that the beam gains after passing through the HW q-plate is $\ell = 2q$.

Equation (1) reveals that the retardance ϕ acts as a tuning parameter between the identity matrix and the HW q-plate matrix, with amplitude factors $\cos(\phi/2)$ and $\sin(\phi/2)$ respectively. Therefore, the action of the device on an input polarization state can be decomposed as a mixing of the input state with the state resulting from the action of a regular q-plate, where the weight of each term depends on the actual retardance of the device. Obviously, when the retardance corresponds to a half wavelength, the Jones matrix in Eq. (1) is exactly $\mathbf{M}_q(\phi = m\pi) = \mathbf{Q}_q$, with m an integer value, and the regular HW q-plate is retrieved. However as stated earlier, in this work we study cases when the retardance is $\phi = +\pi/2$ and $\phi = -\pi/2$ (QW q-plates), where the Jones matrix in Eq. (1) reads:

$$\mathbf{M}_q(\phi = \pm\pi/2) = \frac{1}{\sqrt{2}}\left(\mathbf{I} \pm i\mathbf{Q}_q\right). \tag{3}$$

From this equation it is clear that the vector beam emerging from the QW q-plate, $\mathbf{E}_{out}$, for a given input polarization state, $\mathbf{E}_{in}$, is the superposition of this homogenously polarized input beam $\mathbf{E}_{in}$, with the vector beam generated by the HW q-plate, i.e.:

$$\mathbf{E}_{out} = \mathbf{M}_q \cdot \mathbf{E}_{in} = \frac{1}{\sqrt{2}}\left(\mathbf{I} \pm i\mathbf{Q}_q\right) \cdot \mathbf{E}_{in} = \frac{1}{\sqrt{2}}\left(\mathbf{E}_{in} \pm i\mathbf{Q}_q \cdot \mathbf{E}_{in}\right). \tag{4}$$

The $\pm i$ term in Eq. (4) is a phase delay $\pm\pi/2$ of the beam $\mathbf{Q}_q \cdot \mathbf{E}_{in}$ relative to the input beam $\mathbf{E}_{in}$. The result of this superposition is a hybrid vector beam (HVB) [23]. For example, if LCP is incident onto the device, the output will be a superposition of LCP and RCP with a relative phase shift of $\pm\pi/2$.

In order to get an insight of the resulting polarization patterns, Table 1 shows the Jones vectors for the vector beams generated by the standard HW q-plate and by the QW q-plate, where in both cases a device with q=1 is considered since this is what we use in the experiments. We explicitly write the azimuthal θ dependence of the Jones vectors $\mathbf{E}_{out}(\theta)$ describing the hybrid vector beam exiting the QW q-plate with $\phi = +\pi/2$, and their particular state for azimuth angles θ = 0º, 45º, 90º,

and 135º. And we consider six different input polarization states corresponding to the cardinal points of the Poincaré sphere, i.e., linear states oriented at 0º, 45º, 90º and 135º, and RCP and LCP circular states. For each input polarization, the second column in Table 1 shows the output pure vector beam $\mathbf{Q}_q \times \mathbf{E}_{in}$ emerging from the HW *q*-plate, while the third column shows $\mathbf{E}_{out}(\theta)$ given by (Eq. (4)).

Figure 1 is a pictorial representation of Eq. (4) that illustrates the polarization patterns for the cases considered in Table 1. Each input polarization is drawn in the first column of Fig. 1. Then, the pure vector beam emerging from the standard HW *q*-plate is drawn in the second column. Finally, the hybrid vector beam emerging from the QW *q*-plate is drawn in the third column. These can be understood by adding the contribution of the input polarization and of the output pure vector beam from the HW *q*-plate, with a relative $\pi/2$ phase shift.

Table 1

Jones vectors generated by the standard *q*-plate and by the QW *q*-plate (both with q=1) for different input states. The last four columns show the Jones vector generated by the QW *q*-plate at the azimuth angles θ=0º, 45º, 90º and 135º. The QW *q*-plate with ϕ=+$\pi/2$ is considered.

Input $\mathbf{E}_{in}$	Output from HW *q*-plate $\mathbf{Q}_q \cdot \mathbf{E}_{in}$	Output from QW *q*-plate $\mathbf{E}_{out}$	$\mathbf{E}_{out}(q)$ θ=0	$\mathbf{E}_{out}(q)$ θ=$\pi/4$	$\mathbf{E}_{out}(q)$ θ=$\pi/2$	$\mathbf{E}_{out}(q)$ θ=$3\pi/4$
$\begin{pmatrix}1\\0\end{pmatrix}$	$\begin{pmatrix}\cos(2\theta)\\ \sin(2\theta)\end{pmatrix}$	$\frac{1}{\sqrt{2}}\begin{pmatrix}1+i\cos(2\theta)\\ i\sin(2\theta)\end{pmatrix}$	$e^{i\pi/4}\begin{pmatrix}1\\0\end{pmatrix}$	$\frac{1}{\sqrt{2}}\begin{pmatrix}1\\ i\end{pmatrix}$	$e^{-i\pi/4}\begin{pmatrix}1\\0\end{pmatrix}$	$\frac{1}{\sqrt{2}}\begin{pmatrix}1\\ -i\end{pmatrix}$
$\frac{1}{\sqrt{2}}\begin{pmatrix}1\\1\end{pmatrix}$	$\begin{pmatrix}\cos\left(2\theta-\frac{\pi}{4}\right)\\ \sin\left(2\theta-\frac{\pi}{4}\right)\end{pmatrix}$	$\frac{1}{\sqrt{2}}\begin{pmatrix}\frac{1}{\sqrt{2}}+i\cos\left(2\theta-\frac{\pi}{4}\right)\\ \frac{1}{\sqrt{2}}+i\sin\left(2\theta-\frac{\pi}{4}\right)\end{pmatrix}$	$\frac{e^{i\pi/4}}{\sqrt{2}}\begin{pmatrix}1\\ -i\end{pmatrix}$	$\frac{e^{i\pi/4}}{\sqrt{2}}\begin{pmatrix}1\\1\end{pmatrix}$	$\frac{e^{-i\pi/4}}{\sqrt{2}}\begin{pmatrix}1\\ i\end{pmatrix}$	$\frac{e^{-i\pi/4}}{\sqrt{2}}\begin{pmatrix}1\\1\end{pmatrix}$
$\begin{pmatrix}0\\1\end{pmatrix}$	$\begin{pmatrix}\sin(2\theta)\\ -\cos(2\theta)\end{pmatrix}$	$\frac{1}{\sqrt{2}}\begin{pmatrix}i\sin(2\theta)\\ 1-i\cos(2\theta)\end{pmatrix}$	$e^{-i\pi/4}\begin{pmatrix}0\\1\end{pmatrix}$	$\frac{e^{i\pi/4}}{\sqrt{2}}\begin{pmatrix}1\\ -i\end{pmatrix}$	$e^{i\pi/4}\begin{pmatrix}0\\1\end{pmatrix}$	$\frac{e^{-i\pi/4}}{\sqrt{2}}\begin{pmatrix}1\\ i\end{pmatrix}$
$\frac{1}{\sqrt{2}}\begin{pmatrix}1\\-1\end{pmatrix}$	$\begin{pmatrix}\cos\left(2\theta+\frac{\pi}{4}\right)\\ \sin\left(2\theta+\frac{\pi}{4}\right)\end{pmatrix}$	$\frac{1}{\sqrt{2}}\begin{pmatrix}\frac{1}{\sqrt{2}}+i\cos\left(2\theta+\frac{\pi}{4}\right)\\ \frac{-1}{\sqrt{2}}+i\sin\left(2\theta+\frac{\pi}{4}\right)\end{pmatrix}$	$\frac{e^{i\pi/4}}{\sqrt{2}}\begin{pmatrix}1\\ i\end{pmatrix}$	$\frac{e^{-i\pi/4}}{\sqrt{2}}\begin{pmatrix}1\\-1\end{pmatrix}$	$\frac{e^{-i\pi/4}}{\sqrt{2}}\begin{pmatrix}1\\ -i\end{pmatrix}$	$\frac{e^{i\pi/4}}{\sqrt{2}}\begin{pmatrix}1\\-1\end{pmatrix}$
$\frac{1}{\sqrt{2}}\begin{pmatrix}1\\ i\end{pmatrix}$	$\frac{e^{i2\theta}}{\sqrt{2}}\begin{pmatrix}1\\ -i\end{pmatrix}$	$e^{i(\theta+\pi/4)}\begin{pmatrix}\cos\left(\theta+\frac{\pi}{4}\right)\\ \sin\left(\theta+\frac{\pi}{4}\right)\end{pmatrix}$	$\frac{e^{i\pi/4}}{\sqrt{2}}\begin{pmatrix}1\\1\end{pmatrix}$	$i\begin{pmatrix}0\\1\end{pmatrix}$	$\frac{e^{-i\pi/4}}{\sqrt{2}}\begin{pmatrix}1\\-1\end{pmatrix}$	$\begin{pmatrix}1\\0\end{pmatrix}$
$\frac{1}{\sqrt{2}}\begin{pmatrix}1\\ -i\end{pmatrix}$	$\frac{e^{-i2\theta}}{\sqrt{2}}\begin{pmatrix}1\\ +i\end{pmatrix}$	$e^{-i(\theta-\pi/4)}\begin{pmatrix}\cos\left(\theta-\frac{\pi}{4}\right)\\ \sin\left(\theta-\frac{\pi}{4}\right)\end{pmatrix}$	$\frac{e^{i\pi/4}}{\sqrt{2}}\begin{pmatrix}1\\-1\end{pmatrix}$	$\begin{pmatrix}1\\0\end{pmatrix}$	$\frac{e^{-i\pi/4}}{\sqrt{2}}\begin{pmatrix}1\\1\end{pmatrix}$	$-i\begin{pmatrix}0\\1\end{pmatrix}$

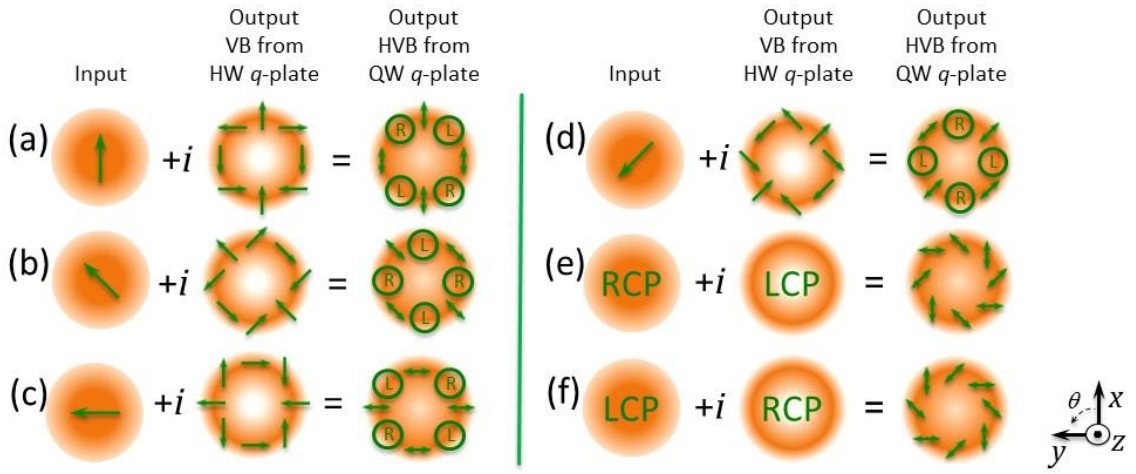

Fig. 1. Pictorial representation of the action of a QW *q*-plate (with *q*=1) on input beams of uniform linear polarization oriented at (a) 0º, (b) 45º, (c) 90º, (d) 135º, and on circular states (e) RCP and (f) LCP. The polarization patterns in the columns correspond, respectively, to: the input beam, the vector beam (VB) produced by the half-wave (HW) *q*-plate, and the resulting hybrid vector beam (HVB) generated by the quarter-wave (QW) *q*-plate (only the case $\phi = +\pi/2$ is drawn).

As an example, let us examine the case in Fig. 1(a), where the input vertical polarization interferes with the pure vector beam of the second-order Poincaré sphere that would be generated by the HW *q*-plate of *q*=1. Note that this pure vector beam is vertically polarized in the horizontal and vertical directions (θ=0º, 90º). Therefore, the superposition of the two beams by the QW *q*-plate yields a hybrid vector beam with linear vertical polarization only along these directions. On the contrary, the pure vector beam emerging form the HW *q*-plate is horizontally polarized at the diagonal directions (θ=±45º). Thus, its superposition with the vertically polarized input beam provides equal field amplitudes in the horizontal and vertical directions. In addition, since there is a $\pi/2$ relative phase shift between them, the resulting hybrid vector beam is circularly polarized in these diagonal directions.

The other situations illustrated in Fig. 1 can be similarly interpreted, and they agree with the Jones vector calculations in Table 1. The cases in Fig. 1(e) and 1(f) are particularly interesting. They correspond to an input circularly polarized beam. Therefore, the output from the HW *q*-plate is circularly polarized with the opposite helicity and exhibits a phase singularity at the beam center. The interference of these RCP and LCP beams with equal weight results in a linearly polarized beam,

but the extra spiral phase difference makes the orientation of the linear state rotate with the azimuth, thus generating a slanted vector beam. However, note that, according to the Jones vectors in Table 1 for these two cases (last two rows), this vector beam rotates the linear polarization as $q\theta$. This is different to the pure vector beams generated by the HW *q*-plate illuminated with a linear state (rows 1 to 4, 2nd column in Table 1), that rotate as $2q\theta$. This effect is similar to that shown in Ref. [18, 24] for a QW metamaterial *q*-plate where the orientation of its fast axis was made slanted in order to generate the radially polarized light beam. Let us note that the linear vector beam in Fig. 1(e) and 1(f) is not pure because the spiral phase is encoded only in one of the two circular polarization components, i.e., it is the slanted version of the equivalent pseudo-radial polarization that was analyzed in Ref. [29]. In general, a rich variety of vector beams, including hybrid vector beams, can be built by collinear superposition of two Laguerre-Gauss modes of orthogonal polarization [30].

As a final remark, it's worth noting that whereas standard HW *q*-plates can be combined with HW plates to build effective HW *q*-plates of higher or lower *q*-value [31], such arithmetic is not possible to perform with QW *q*-plates. Simple algebraic calculations considering the QW *q*-plate matrix in Eq. (3) and the properties described in [31] show that no such combinations of QW *q*-plates are possible because of crossed terms from the two parts in Eq. (3).

3. SPECTRAL CHARACTERIZATION OF THE Q-PLATE

The spectral characterization of the retardance in standard linear retarders is usually done by placing the device between linear polarizers oriented at ±45º to the principal axis [32]. However, for a *q*-plate this is not a practical solution because of the rotation of the retarder axis with the azimuthal angle. Instead, the retardance can be examined by generating and detecting left and right circularly polarized light. Therefore, the *q*-plate must be placed in between crossed or parallel circular polarizers. Since the matrix $\mathbf{Q}_q$ in Eq. (2) yields the opposite circular state when illuminated with circular polarization, Eq. (1) shows that the normalized transmitted intensity of the *q*-plate placed in between crossed circular polarizers is given by:

$$i_{cros}(\phi) = \sin^2(\phi/2). \quad (5)$$

Since the retardance varies with wavelength as $\phi(\lambda)$, the spectral transmission measurements can be used to determine the *q*-plate retardance through this equation.

We have characterized, in a broad spectral range, the retardance and the performance of a commercial *q*-plate from Thorlabs (zero-order vortex half-wave retarder, model WPV10-633) of q=1 and 633 nm nominal operating wavelength. Figure 2(a) shows a scheme of the optical set-up employed for its spectral characterization, which is adapted from a previous system to characterize homogeneous retarders in a broad spectral range [33]. The *q*-plate, which is placed between crossed or parallel broadband circular polarizers, is illuminated with light of a continuous spectrum, and the light transmitted by the system is analyzed by means of a spectrometer.

The method is equivalent to that used in [16] but, there, a monochromatic laser was employed as light source and the retardance was changed electrically since a tunable liquid-crystal *q*-plate was employed. Here instead, the *q*-plate is static and the wavelength is the tuning parameter for the retardance. As a light source, we use a quartz tungsten halogen lamp (Oriel, model 66882) with power adjustable from 10 to 250 watts. It provides white light of continuous broadband spectrum. The housing includes a fused silica condenser that can be adjusted to provide a collimated beam of 33 mm diameter.

We built the broadband circular polarizers combining quarter-wave Fresnel rhombs and broadband linear polarizers. Fresnel rhombs are optical retarders that exhibit almost constant retardance in a wide spectral range [33]. We use two quarter-wave Fresnel rhombs (Thorlabs, model FR600QM) with 400 nm-1550 nm wavelength operating range. We combine them with two Glan-Taylor linear polarizers from Edmund Scientific, which operate in the range from 350 nm to 2200 nm. This way we can build two broadband circular polarizers, by orienting the linear polarizers at 45º with respect to the rhomb neutral axes.

The light transmitted by the system is captured by an optical fiber which directs it to a spectrometer (Stellar-Net, model STN-BLK-C-SR) which measures the spectrum in the range from 200 nm to 1080 nm with a resolution of 2 nm.

The spectrum of the transmitted light was measured for two configurations: with parallel and with crossed circular polarizers. Figure 2(b) shows the normalized spectral transmission, obtained by dividing each transmission curve (with crossed or parallel polarizers) by the addition of the two curves. The normalized transmission shows the characteristic oscillating behaviour as a function of wavelength of a zero-order retarder. This result confirms that the *q*-plate operates with π retardation for a wavelength plateau around 633 nm.

However, note that there are two wavelengths where the curves for parallel and crossed circular polarizers will cross. These crossings indicate the wavelengths where the retardance is quarter-wavelength. One crossing lies in the near IR range, slightly out of the spectral range we can measure, whose maximum wavelength is 1080 nm. The second crossing lies in the blue region of the spectrum, at 475 nm. In between, let us remark the wavelength plateau of almost 100 nm that is centered at 650 nm, denoting the HW *q*-plate operation.

We assumed a spectral retardance function $\phi(\lambda)$ that follows the typical retardance versus wavelength variation of a single-layer retarder, where ϕ monotonically decreases with λ. We use this retardance function to numerically fit the transmission of our set-up. The calculated transmission is then fit to the experimental curves to retrieve the parameters that describe the retardance function $\phi(\lambda)$. The best fit for the transmission is included in Fig. 2(b), practically overlapping the experimental data. The retrieved function $\phi(\lambda)$ is shown in Fig. 2(c) and indicates a retardance $\phi=\pi/2$ at 1130 nm, $\phi=\pi$ around 633 nm and $\phi=3\pi/2$ at 475 nm.

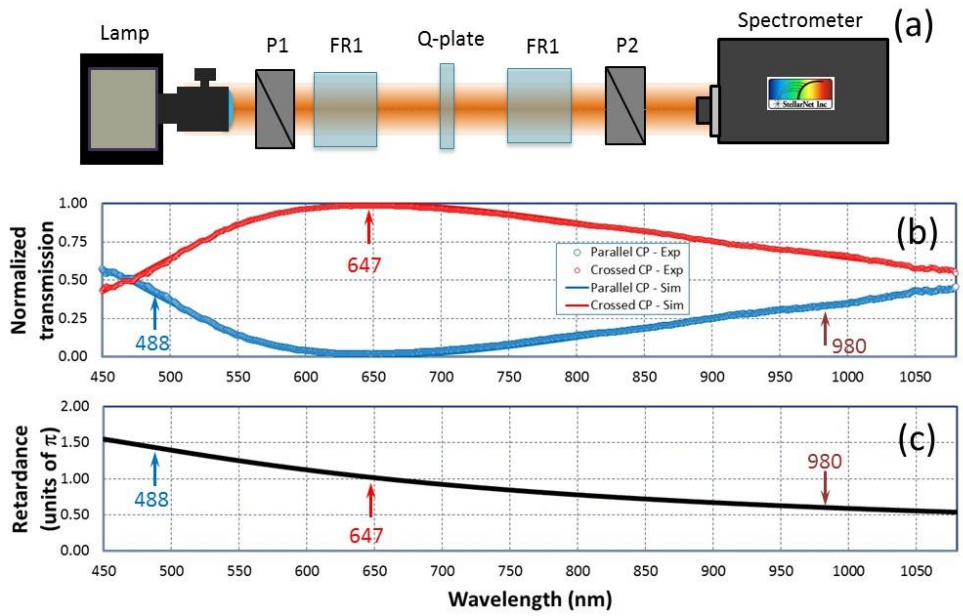

Fig. 2. (a) Optical system for the spectral characterization of the q-plate. P: linear polarizers, FR: Fresnel rhombs. (b) Normalized spectral transmission of the *q*-plate in between parallel and crossed circular polarizers. Experimental data and numerical fit are included for comparison. (c) Spectral retardance $\phi(\lambda)$ of the q-plate after fitting the data in (b). The operating wavelengths employed in this work are indicated by arrows.

Next, we will present experimental results on the generation of vector beams with this commercial and static *q*-plate of *q*=1 using three wavelengths from available monochromatic lasers that provide retardances close enough to π, $3\pi/2$ and $\pi/2$, respectively. First, we will verify the generation of vector beams in the second-order Poincaré sphere by illuminating the device with a laser line of 647 nm wavelength. Next, we will show that this *q*-plate can work as a QW spatially-variable retarder at two other wavelengths (488 nm and 980 nm).

4. PURE VECTOR BEAMS GENERATED AT THE DESIGN WAVELENGTH

We start by illustrating the operation of our device as a HW *q*-plate for a wavelength close to the nominal design wavelength indicated by the manufacturer, 633 nm. For that purpose, we illuminate the *q*-plate with a collimated beam from an Ar-Kr laser, and filter the red line of 647 nm. Figure 3 shows the experimental output obtained by the CCD camera following an approach similar to previous works [16]. We illuminate the *q*-plate with a given homogeneous input polarization state (linear states oriented vertical, horizontal and at ±45º, and RCP and LCP states), and for each case we

capture the beam when a polarizer analyzer is placed in front of the CCD detector and its transmission axis is successively oriented to detect the same six previous states of polarization. When required, circular polarizers are built by combining a linear polarizer and a quarter-wave plate suitable at 647 nm.

The results in Fig. 3 show the expected behaviour of a standard *q*-plate with π retardance and *q*=1 [5, 34], since, as we shall discuss below, they agree with the polarization patterns in the second column of Fig. 1. These patterns are drawn again in Fig. 3 to check the experimental polarization distribution of the CCD captures. When the *q*-plate is illuminated with a linear state (rows 3(a) to 3(d)), the output is a beam with linear polarizations that rotate two cycles with the azimuth (since *q*=1). These beams correspond to the cardinal points located on the equator of the second-order Poincaré sphere. This is visible when we use a linear analyzer, since the beam gets completely extinguished at four angular directions in each case. When the circular analyzers are employed, a uniform transmission is obtained. The axial singularity is clearly visible in in both RCP and LCP components.

On the contrary, when the *q*-plate is illuminated with circular polarization, the output is also circularly polarized, but with the opposite helicity. This is shown in rows 3(e) and 3(f). Note how now the transmitted beam is completely extinguished for one circular analyzer, while it is completely transmitted for the opposite circular analyzer. In addition, the data shows how the transmission is uniform for any linear analyzer. The two vector beams generated in this way correspond to the poles of the second-order Poincaré sphere. Therefore, these results prove that this commercial device operates as a HW *q*-plate for a wavelength of 647 nm, which is very close to the nominal design wavelength indicated by the manufacturer. We can conclude that this behaviour will be kept for wavelengths in the approximate range of $650\ \mathrm{nm} \pm 50\ \mathrm{nm}$, according to the plateau in Fig. 2(b).

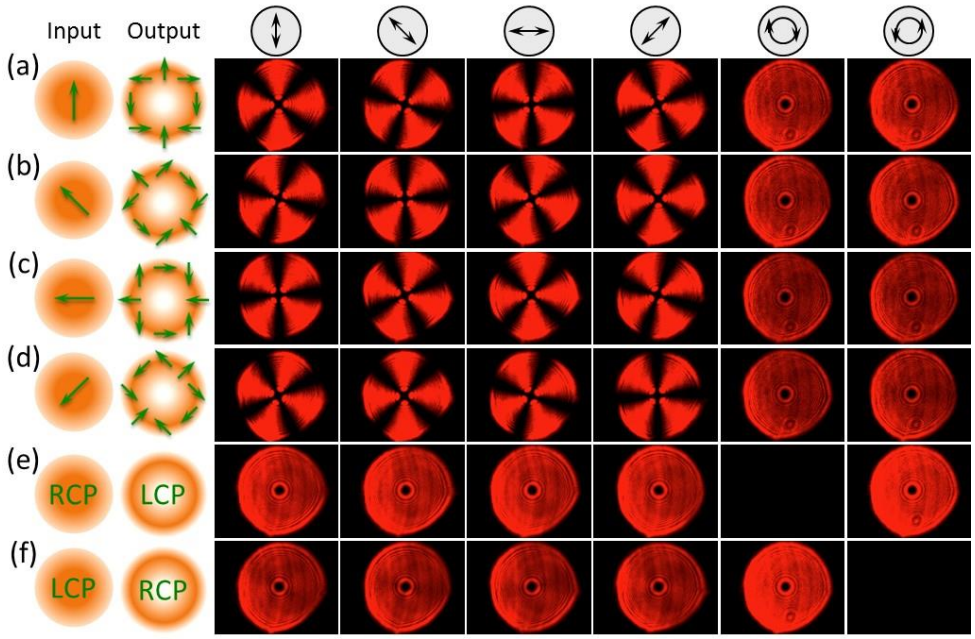

Fig. 3. Experimental realization of second-order vector beams by illuminating a commercial *q*-plate of *q*=1 with a wavelength of 647 nm and π retardance at this wavelength. Each row corresponds to the output vector beam drawn in the second column, which is obtained for input linear states at 0º, 45º, 90º, and 135º, and RCP and LCP circular states respectively. The analyzer is indicated on top.

5. HYBRID VECTOR BEAMS GENERATED AT THE QUARTER-WAVE RETARDANCE

Next, the same commercial *q*-plate is employed with two other available laser sources: an Ar-Kr laser operating at the blue line of 488 nm, and an IR laser diode of wavelength 980 nm. These wavelengths are close enough to the values in Fig. 2(c) that yield quarter-wave retardance. For each case, we present the experimental results as well as the corresponding polarization pattern, and compare them with the *q*-plate theory. We distinguish between these two wavelengths, since the *q*-plate quarter-wave retardance is of opposite sign in each case (the three-quarter-wave plate is equivalent to a negative quarter-wave plate). Consequently, the vector beams generated at these two wavelengths will show differences. Since the 488 nm wavelength lies much closer to the crossing of the two curves in Fig. 2(b) signaling quarter-wave operation than 980 nm does, we will first show this case.

5.1. Q-plate operation at the negative quarter-wave retardance

Let us now demonstrate the operation of our commercial device as a *q*-plate with $-\pi/2$ retardance. We use the 488 nm wavelength of our Ar-Kr laser in the same setup used in section 4 by simply

changing the interference filter in order to select this blue wavelength. According to Fig. 2(c), the retardance at 488 nm is very close to $3\pi/2$ radians, or equivalently, to negative quarter-wave retardance.

As in the previous case, we illuminate the *q*-plate with the six input cardinal states of polarization, and, for each case, we capture the pattern with six analyzers transmitting each of these six cardinal states. The results are presented in Fig. 4, where we draw the expected polarization patterns following the procedure explained in section 2. The captured experimental data agree well with the expected states of polarization shown in the second column of Fig. 4.

Let us note that by illuminating the device with input linear polarization, hybrid vector beams are generated where the local polarization changes from linear to elliptical and to pure circular with the azimuth angle across the beam section. Note that the intensity patterns obtained when the analyzer is crossed to the input polarization (see panels marked with a yellow cross) are equivalent to those obtained for the HW *q*-plate operation in Fig. 3. This shows that the device is operating as indicated in Eq. (3), namely, as a combination of the identity matrix and a HW *q*-plate. When the analyzer is perpendicular to the input polarization only the action of the HW *q*-plate term remains, and this is why these captures are identical in Figs. 3 and 4.

On the other hand, when illuminating the device with input circularly polarized light (two last rows in Fig. 4), the output beam shows transmission for both circular analyzers (in contrast to the case in Fig. 3 where only one circular component is present). The phase singularity is present only in the circular component opposite to the input circular polarization. The resulting beam is a slanted pseudo-vector beam [29]. Note that the intensity of the four images captured for input circular polarizers/output circular analyzers is pretty much the same. This indicates that the weight of the identity term and the HW *q* plate term in Eq. (1) is almost equal, and consequently, it means that at 488 nm the retardance is practically $3\pi/2$.

Also remarkable is the pattern around the singularity adopting the typical S shape [18, 24, 25] when the input beam is circularly polarized and the output beam is analyzed with a linear analyzer,

or viceversa. This swerving pattern is due to the interference of the plane-wave component with the vortex beam component, as described in Eq. (4). Therefore, these results verify that our commercial device operates as a negative-QW *q*-plate for a wavelength of 488 nm.

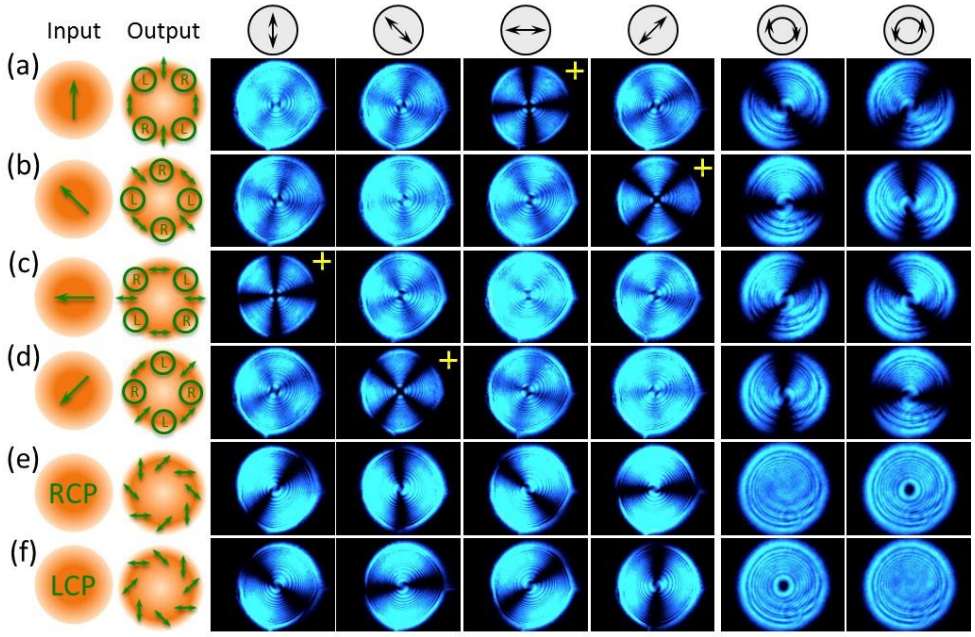

Fig. 4. Experimental results for wavelength 488 nm and a commercial *q*-plate of q=1 and $3\pi/2$ retardance at this wavelength. Each row corresponds to the output vector beam drawn in the second column, which is obtained for input linear states at 0º, 45º, 90º, and 135º, and RCP and LCP circular states respectively. The final analyzer is indicated on top.

5.2. Q-plate operation at the positive quarter-wave retardance

Finally, let us demonstrate the operation of our commercial device as a *q*-plate with $+\pi/2$ retardance. The optical set-up is similar to that in [17] where an IR laser of 1550 nm was employed. Here, instead, a collimated beam from an IR laser diode (BWTEK BRM Light Source) emitting at 980 nm illuminates the *q*-plate. According to Fig. 1, this wavelength is close enough to approximate the positive QW retardance in our device. As quarter waveplates designed to operate at this wavelength were not available, we used Soleil-Babinet compensators that need to be carefully calibrated together with Glan-Taylor linear polarizers, in order to build our input and output circular polarizers. The q-plate was then sandwiched between two pairs of linear polarizer-Soleil-Babinet compensators and the whole set of six by six input/output polarization states was characterized, where the transmitted beam was imaged onto a SONY model XC-37 CCD Video Camera.

The results displayed in Fig. 5 show similar intensity patterns as in the previous case. Their analysis reveals that they correspond to vector beams with polarization distribution as in Fig. 1. As in the case of the negative-QW q-plate, the captures with crossed linear polarizers, which provide intensity patterns equivalent to those of the HW *q*-plate (Fig. 3), are again marked with a yellow arrow. However, the positive sign of the retardance produces minor changes in the generated hybrid vector beams with respect to those in Fig. 4. For instance, RCP and LCP states are switched in Fig. 5 with respect to Fig. 4, and the pseudo-slanted states generated for input circular polarizations rotate in the opposite sense in comparison to those in Fig. 4. Finally, let us remark that since 980 nm is further from the $+\pi/2$ retardance than 488 nm is from the $3\pi/2$ retardance, we can notice the shift in intensity between the four images of circularly polarized input and output states. Namely, the pair of images where the analyzer matches the input's handedness is dimmer than the image where the input and analyzer are of opposite handedness. But, again, these results confirm the theoretical predictions and show the possibilities of using this commercial *q*-plate as a QW *q*-plate for generating hybrid vector beams.

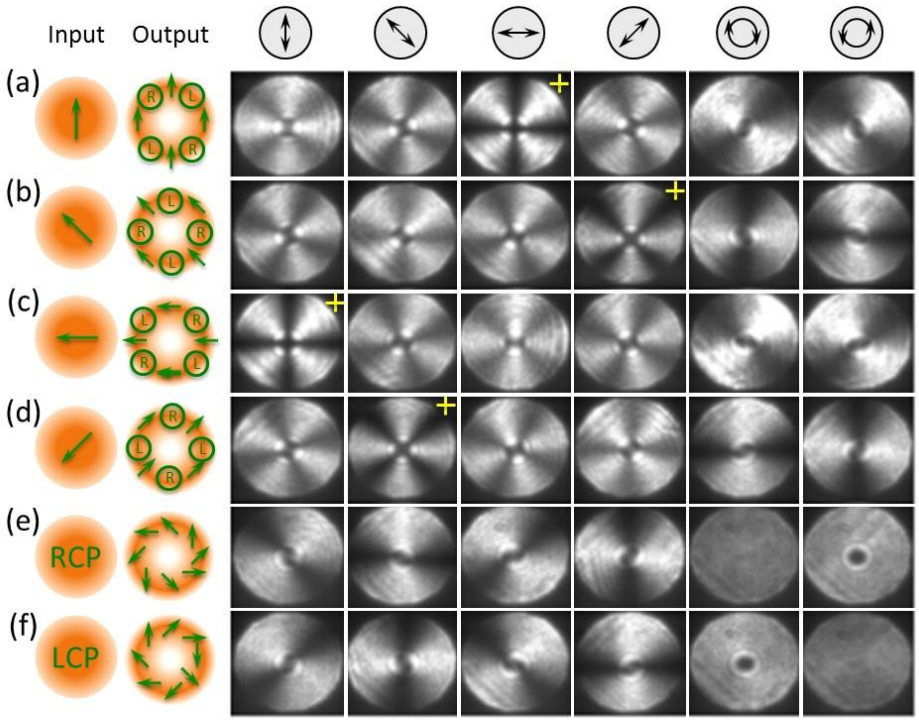

Fig. 5. Experimental results for wavelength 980 nm and a commercial *q*-plate of q=1 and $\pi/2$ retardance at this wavelength. Each row corresponds to the output vector beam drawn in the second column, which is obtained for input linear states at 0º, 45º, 90º, and 135º, and RCP and LCP circular states respectively. The final analyzer is indicated on top.

6. CONCLUSIONS

In conclusion, we have characterized the spectral transmission of a commercial non-tunable liquid-crystal polymer *q*-plate, or vortex retarder, originally designed to operate as a spatially-variant half-wave retarder at 633 nm. This characterization was done in a wide broadband range, from 400 nm to 1080 nm, using quarter-wave Fresnel rhombs and linear polarizers to build broadband circular polarizers. As a result of this spectral characterization, we could conclude that the same device can operate as a spatially-variant quarter-wave *q*-plate, with retardances close to $3\pi/2$ and $\pi/2$, for wavelengths 488 nm and 980 nm, respectively. The device is modelled using the Jones matrix formalism, and the resulting polarization distribution across the beam section is retrieved for various input polarizations. Experimental results illuminating the device with the red and blue lines of an Ar-Kr laser (647 nm and 488 nm) and with an IR laser diode (980 nm) confirm the predicted behaviour.

These results are interesting because they show that we can use the same static *q*-plate to generate radial and azimuthal vector beams by either illuminating the device with linearly polarized light of 647 nm or by illuminating it with circularly polarized light of 488 nm or 980 nm. In these latter the vector beams are pseudo-radial, the optical singularity appears in only one of the circular components, and the polarization azimuthal rotation is of only $q\theta$ (instead of $2q\theta$, as in the standard HW *q*-plate).

Remarkably, we have also shown the generation of hybrid vector beams when illuminating the device with linearly polarized light of wavelengths 488 nm and 980 nm, for which the retardance is close to $3\pi/2$ and $\pi/2$. These particular cases of vector beams, where the ellipticity changes along the azimuthal angle, were demonstrated from a regular metamaterial HW *q*-plate cascaded with a spiral-phase plate [25] and also from a spun elliptical core optical fiber [35], and have been proposed for particle trapping applications and geometric phase studies.

Let us note that our study did not consider propagation effects, but rotation of the polarization patterns may occur due to Gouy phase effects [36].

In summary, this work demonstrates the versatility of static commercial q-plates for generating vector beams in different wavelength ranges, which can widen the applications of these devices. For instance, pure and hybrid vector beams could be simultaneously generated at the red line and blue line of the Ar-Kr laser used in this work for coherent multicoloured vector beam multiplexing. In addition, the vector beam in the red line channel could be further manipulated using a configuration in reflection and a quarter-wave plate to double its topological charge [34].

Acknowledgements

MMSL and IM acknowledge support from Ministerio de Economía y Competitividad from Spain (ref. FIS2015-66328-C3-3-R) and from Conselleria d'Educació, Investigació, Cultura i Esport, Generalitat Valenciana (ref. PROMETEO-2017-154).

References

1. L. Marrucci, C. Manzo, and D. Paparo, “Optical spin-to-orbital angular momentum conversion in inhomogeneous anisotropic media,” *Phys. Rev. Lett.* **96**, 163905 (2006).
2. M. Stalder and M. Schadt, “Linearly polarized light with axial symmetry generated by liquid-crystal polarization converters,” *Opt. Lett*. **21**, 1948-1950 (1996).
3. A. Niv, Y. Gorodetski, V. Kleiner, and E. Hasman, “Topological spin–orbit interaction of light in anisotropic inhomogeneous subwavelength structures,” *Opt. Lett.* **33**, 2910-2912 (2008).
4. S. Slussarenko, B. Piccirillo, V. Chigrinov, L. Marrucci, and E. Santamato, “Liquid crystal spatial-mode converters for the orbital angular momentum of light”, *J. Opt*. **15**, 025406 (2013).
5. E. Karimi, S. Slussarenko, B. Piccirillo, L. Marrucci, and E. Santamato, “Polarization-controlled evolution of light transverse modes and associated Pancharatnam geometric phase in orbital angular momentum”, *Phys. Rev. A* **81**, 053813 (2010).
6. G. Milione, T. A. Nguyen, J. Leach, D. A. Nolan, and R. R. Alfano, "Using the nonseparability of vector beams to encode information for optical communication", *Opt. Lett*. **40**, 4887-4890 (2015).
7. G. Milione, A. Dudley, T. A. Nguyen, K. Chakraborty, E. Karimi, A. Forbes, and R. R. Alfano, “Measuring the self-healing of the spatially inhomogeneous states of polarization of vector Bessel beams”, *J. Opt.* **17**, 035617 (2015).
8. J. Davis, I. Moreno, K. Badham, M. M. Sánchez-López, and D. M. Cottrell, “Nondiffracting vector Bessel beams where the charge and the polarization state vary with propagation distance”, *Opt. Lett*. **41**, 2270-2273 (2016).
9. G. Milione, M. P. J. Lavery, H. Huang, Y. Ren, G. Xie, T. A. Nguyen, E. Karimi, L. Marrucci, D. A. Nolan, R. R. Alfano, and A. E. Willner, “4x20 Gbit/s mode division multiplexing over free space using vector modes and a q-plate mode (de)multiplexer”, *Opt. Lett*. **40**, 1980-1983 (2015).

10. L. Marrucci, “Liquid crystal *q*-plates: classical and quantum photonic applications”, *Proc. SPIE* 8475, 84750P (2012).
11. B. J. Roxworthy and K. C. Toussaint, Jr., “Optical trapping with π-phase cylindrical vector beams”, *New J. Phys*. **12**, 073012 (2010).
12. L. Rao, J. Pu, Z. Chen, and P. Yei, “Focus shaping of cylindrically polarized vortex beams by a high numerical-aperture lens”, *Opt. Laser Technol*. **41**, 241-246 (2009).
13. B. S. Bhargava Ram, P. Senthilkumaran, and A. Sharma, “Polarization-based spatial filtering for directional and nondirectional edge enhancement using an S-waveplate”, *Appl. Opt*. **56**, 3171-3178 (2017).
14. S. R. Nersisyan, N. V. Tabiryan, D. Mawet, and E. Serabyn, “Improving vector vortex waveplates for high-contrast coronagraphy”, *Opt. Express* **21**, 8205-8213 (2013).
15. S. Slussarenko, A. Murauski, T. Du, V. Chigrinov, L. Marrucci, and E. Santamato, “Tunable liquid crystal q-plates with arbitrary topological charge,” *Opt. Express* **19**, 4085-4090 (2011).
16. J. A. Davis, N. Hashimoto, M. Kurihara, E. Hurtado, M. Pierce, M. M. Sánchez-López, K. Badham, and I. Moreno, “Analysis of a segmented q-plate tunable retarder for the generation of first-order vector beams”, *Appl. Opt.* **54**, 9583-9590 (2015).
17. K. Badham, S. Delaney, N. Hashimoto, M. M. Sánchez-López, M. Kurihara, A. Tanabe, I. Moreno, and J. A. Davis, “Generation of vector beams at 1550 nm telecommunications wavelength using a segmented q-plate”, *Opt. Eng.* **55**, 030502 (2016).
18. M. Beresna, M. Gecevičius, P. G. Kazansky, and T. Gertus, “Radially polarized optical vortex converter created by femtosecond laser nanostructuring of glass,” *Appl. Phys. Lett*. **98**, 201101 (2011).
19. Y. Liu, X. Ling, X. Yi, X. Zhou, H. Luo, and S. Wen, “Realization of polarization evolution on higher-order Poincaré sphere with metasurface,” *Appl. Phys. Lett.* **104**, 191110 (2014).
20. C. Loussert, K. Kushnir, and E. Brasselet, “Q-plates micro-arrays for parallel processing of the photon orbital angular momentum”, *Appl. Phys. Lett*. **105**, 121108 (2014).

21. E. Karimi, B. Piccirillo, E. Nagali, L. Marrucci, and E. Santamato, “Efficient generation and sorting of orbital angular momentum eigenmodes of light by thermally tuned q-plates”, *Appl. Phys. Lett*. **94**, 231124 (2009).

22. Y. S. Rumala, G. Milione, T. A. Nguyen, S. Pratavieira, Z. Hossain, D. Nolan, S. Slussarenko, E. Karimi, L. Marrucci, and R. R. Alfano, “Tunable super-continuum light vector vortex beam generator using a *q*-plate,” *Opt. Lett.* **38**, 5083-5086 (2013).

23. F. Cardano, F. Massa, H. Qassim, E. Karimi, S. Slussarenko, D. Paparo, C. de Lisio, F. Sciarrino, E. Santamato, R. Boyd, and L. Marrucci, “Quantum walks and wavepacket dynamics on a lattice with twisted photons”, *Sci. Adv*. **1**, e1500087 (2015).

24. W. Shu, X. Ling, X. Fu, Y. Liu, Y. Ke, and H. Luo, “Polarization evolution of vector beams generated by *q*-plates”, *Photon. Res*. **5**, 64-72 (2017).

25. Z. Liu, Y. Liu, Y. Ke, Y. Liu, W. Shu, H. Luo, and S. Wen, “Generation of arbitrary vector vortex beams on hybrid-order Poincaré sphere”, *Photon. Res.* **5**, 15-21 (2017).

26. S. Mamani, E. Bendau, J. Secor, S. Ashrafi, J. J. Tu, and R. R. Alfano, “Hybrid generation and analysis of vector vortex beams”, *Appl. Opt*. **56**, 2171-2175 (2017).

27. L. Yan, P. Gregg, E. Karimi, A. Rubano, L. Marrucci, R. Boyd, and S. Ramachandran, “Q-plate enabled spectrally diversed orbital-angular-momentum conversion for stimulated emission depletion microscopy”, *Optica* **2**, 900-903 (2015).

28. J. E. Holland, I. Moreno, J. A. Davis, M. M. Sánchez-López, and D. M. Cottrell, “Q-plates with a nonlinear azimuthal distribution of the principal axis: application to encoding binary data”, *Appl. Opt*. **57**, 1005-1010 (2018).

29. J A. Davis, D. M. Cottrell, B. C. Schoonover, J. B. Cushing, J. Albero, and I. Moreno, “Vortex sensing analysis of radially and pseudo-radially polarized beams”, *Opt. Eng.* **52**, 050502 (2013).

30. E. J. Galvez, S. Khadka, W. H. Schubert, and S. Nomoto, "Poincaré-beam patterns produced by nonseparable superpositions of Laguerre–Gauss and polarization modes of light", *Appl. Opt*. **51**, 2925-2934 (2012).

31. S. Delaney, M. M. Sánchez-López, I. Moreno, and J. A. Davis, "Arithmetic with *q*-plates", *Appl. Opt.* **56**, 596-600 (2017).

32. M. Emam-Ismail, "Spectral variation of the birefringence, group birefringence and retardance of a gypsum plate measured using the interference of polarized light", *Opt. Laser Technol.* **41**, 615-621 (2009).

33. A. Messaadi, M. M. Sánchez-López, P. García-Martínez, A. Vargas, and I. Moreno, "Optical system for measuring the spectral retardance function in an extended range", *J. Eur. Opt. Soc. – Rapid Pub.* **12**, 21 (2016).

34. M. M. Sánchez-López, J. A. Davis, N. Hashimoto, I. Moreno, E. Hurtado, K. Badham, A. Tanabe, and S. Delaney, "Performance of a *q*-plate tunable retarder in reflection for the switchable generation of both first- and second-order vector beams", *Opt. Lett*. **41**, 13-16 (2016).

35. G. Milione, H. I. Sztul, and R. R. Alfano, "Stokes polarimetry of a hybrid vector beam from a spun elliptical core optical fiber", *Proc. SPIE* **7613**, 761305 (2010).

36. G. M. Philip, V. Kumar, G. Milione, and N. K. Viswanathan, "Manifestation of the Gouy phase in vector-vortex beams", *Opt. Lett.* **37**, 2667-2669 (2012).